Anisotropic dynamics of water ultraconfined in macroscopically oriented channels of single-crystal beryl: A multifrequency analysis

Lawrence M. Anovitz,[1] Eugene Mamontov,[2] Paul ben Ishai,[3] and Alexander I. Kolesnikov[2]

[1]*Chemical Sciences Division, MS 6110, P.O. Box 2008, Oak Ridge National Laboratory, Oak Ridge, Tennessee 37831-6110, USA*

[2]*Chemical and Engineering Materials Division, MS 6473, P.O. Box 2008, Oak Ridge National Laboratory, Oak Ridge, Tennessee 37831-6473, USA*

[3]*Department of Applied Physics, The Hebrew University of Jerusalem, Givat Ram, 91904 Jerusalem, Israel*

(Received 27 February 2013; revised manuscript received 9 August 2013; published 8 November 2013)

The properties of fluids can be significantly altered by the geometry of their confining environments. While there has been significant work on the properties of such confined fluids, the properties of fluids under ultraconfinement, environments where, at least in one plane, the dimensions of the confining environment are similar to that of the confined molecule, have not been investigated. This paper investigates the dynamic properties of water in beryl ($Be_3Al_2Si_6O_{18}$), the structure of which contains approximately 5-Å-diam channels parallel to the *c* axis. Three techniques, inelastic neutron scattering, quasielastic neutron scattering, and dielectric spectroscopy, have been used to quantify these properties over a dynamic range covering approximately 16 orders of magnitude. Because beryl can be obtained in large single crystals we were able to quantify directional variations, perpendicular and parallel to the channel directions, in the dynamics of the confined fluid. These are significantly anisotropic and, somewhat counterintuitively, show that vibrations parallel to the *c*-axis channels are significantly more hindered than those perpendicular to the channels. The effective potential for vibrations in the *c* direction is harder than the potential in directions perpendicular to it. There is evidence of single-file diffusion of water molecules along the channels at higher temperatures, but below 150 K this diffusion is strongly suppressed. No such suppression, however, has been observed in the channel-perpendicular direction. Inelastic neutron scattering spectra include an intramolecular stretching O-H peak at ∼465 meV. As this is nearly coincident with that known for free water molecules and approximately 30 meV higher than that in liquid water or ice, this suggests that there is no hydrogen bonding constraining vibrations between the channel water and the beryl structure. However, dielectric spectroscopic measurements at higher temperatures and lower frequencies yield an activation energy for the dipole reorientation of 16.4 ± 0.14 kJ/mol, close to the energy required to break a hydrogen bond in bulk water. This may suggest the presence of some other form of bonding between the water molecules and the structure, but the resolution of the apparent contradiction between the inelastic neutron and dielectric spectroscopic results remains uncertain.

DOI: 10.1103/PhysRevE.88.052306 PACS number(s): 78.70.Nx, 25.40.Dn, 77.22.−d

I. INTRODUCTION

The nature of fluid-solid interactions is an important question in both geology and materials science, as their interfacial properties control many reactive and recrystallization processes. An important subset of this problem is the analysis of the structure and dynamics of water, or other fluids, in confined systems. It is well known that the properties of fluids under such conditions (see, e.g., Ref. [1]) are significantly different from those of bulk fluids. However, studies of confined fluids have been largely limited to porous media with pore sizes above 1 nm as a confining matrix, that is, mesoporous materials, although there does exist a significant class of crystalline materials that contain structural channels significantly smaller than those in mesoporous solids, yet large enough to host substantial quantities of fluids (see Ref. [2]). Because the diameter of the confining channels (<1 nm) is not much bigger than that of the confined molecule, we refer to fluids confined in such systems as ultraconfined.

The opportunity to use single crystals of such minerals to study anisotropy in the microscopic dynamics of ultraconfined water in macroscopically oriented channels is intriguing. The anisotropy in the macroscopic dynamics, which manifests itself in an anisotropic long-range translational diffusion coefficient, is known in the confinement of limited dimensionality. However, the anisotropy in microscopic dynamics, such as the anisotropic relaxation times associated with elementary diffusion jumps of confined liquid molecules, is much more difficult to observe. Mamontov *et al.* [3,4] measured the microscopic dynamics of water and benzene confined in macroscopically oriented nanochannels of chrysotile asbestos fibers using quasielastic neutron scattering (QENS). The diameter of these channels was about 5 nm and the jump diffusion relaxation time was found to be isotropic (the same in the directions parallel and perpendicular to the channels axis) not only for water molecules [3], but also for the larger benzene molecules [4]. They concluded that in order for the anisotropy in the microscopic dynamics to be observable the diameter of the nanochannels should be not much greater than that of the confined molecules, provided all the nanochannels could be oriented macroscopically with respect to the probe. To date, such conditions for experimental studies of confined liquids have been satisfied only for two-dimensional confinement in layered systems such as various micas [5–11].

Fluids in other systems, such as hydration water on the surface of oxide nanoparticles [12–17] or water in zeolites [18–22], also likely experience ultraconfinement in some dimensions (perpendicular to the surface or the channels axis).

In these systems, the anisotropy in the relaxation times of confined molecules is suggested by simulations, but cannot be verified experimentally, because macroscopically aligned samples with suitably large surface areas are not available, and powder samples have to be studied instead. This precludes direct probing of relaxation anisotropy, even if it is indeed induced by the ultraconfinement.

In this paper, we report the results of a study of the anisotropy of the microscopic dynamics of water in the channels of beryl using QENS and inelastic neutron scattering (INS) and dielectric spectroscopy. These techniques cover distinctly different frequency ranges and thus different types of motions of the channel water. Beryl is available as either a natural or a synthetic material in large single crystals, thereby allowing studies in which all of the channels are oriented in a given direction with respect to the probe. Macroscopically oriented single crystals of beryl therefore provide a rare opportunity to directly probe the anisotropy of the relaxation times and vibrational spectra of confined molecules (in this study, water) due to ultraconfinement.

II. BACKGROUND

The structure of beryl (nominally $Be_3Al_2Si_6O_{18}$) is hexagonal (Fig. 1) and built around continuous sixfold channels of silica tetrahedra parallel to the c axis. The rings that form the channels have a diameter of approximately 4.86 Å. Beryl is known to contain guest cations in these channels, most commonly Na and Cs, as well as up to 2 wt.% water [23]. The rings consist solely of silica tetrahedra, with Al tetrahedra and Be octahedra lying between the rings. Thus water in the ring channels is directly coordinated only to the silica tetrahedra. Various structural substitutions also occur, including Fe^{2+}, Mg, and Mn^{2+} for Al and Li^{+} for Be. Water in the channels occurs in two orientations. Type-I water has its H-H axis parallel to the c axis of the beryl and is commonly present in alkali-metal-free beryls, while type-II water has its H-H axis perpendicular to c and is commonly present in sodium-rich beryls. Other alkali-metal-rich beryls contain hydroxyl groups in the channels [24–32].

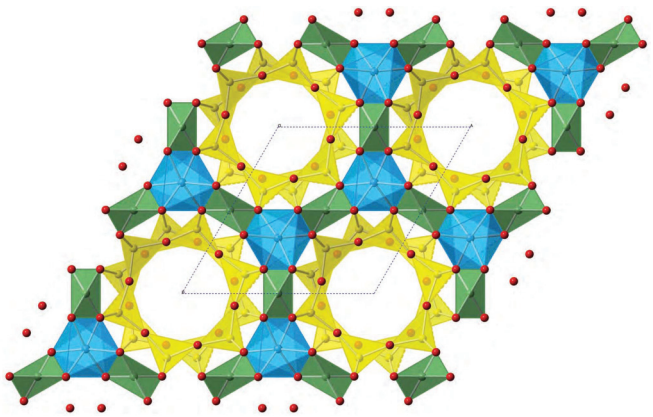

FIG. 1. (Color) Structure of beryl ($Be_3Al_2Si_6O_{18}$) showing large open channels running parallel to the crystallographic c axis (out of the figure's plane): Si, yellow; Al, blue; O, red; and Be, green. The dimension of the unit cell perpendicular to the c axis is $a = 9.21$ Å, as shown.

III. EXPERIMENTAL METHODS

We have used three techniques to probe the anisotropy in the dynamics of water in the channels in beryl: INS, QENS, and dielectric spectroscopy (DS). Combining these techniques permits us to study a wide variety of dynamical motions as each is sensitive to a different frequency range. Inelastic neutron scattering is sensitive to intramolecular vibrational and intermolecular translational and librational motions on the 10^{-15}–10^{-12} s time scale, QENS to translational or rotational motions on the 10^{-12}–10^{-9} s time scale, and DS to cooperative, collective motions on a 10^{-6}–10 s time scale. Thus, while there are some gaps and limited overlap, these three techniques can provide information on the motions of confined water molecules at time scales covering approximately 16 orders of magnitude.

Neutron scattering has been widely used in studies of water dynamics. This is because of the large incoherent neutron scattering cross section of hydrogen compared to other elements, which allows obtaining scattering spectra dominated by the scattering from hydrogen-containing species in confinement rather than from the confining matrix. Inelastic neutron scattering is particularly suitable for investigations of intermolecular translational (0–40 meV) and librational (40–140 meV) vibrational bands and intramolecular H-O-H bending (around 205 meV) and O-H stretching (400–470 meV) modes of water molecules (motions on time scales from approximately 10^{-12} to 10^{-15} s, 1 meV equal to 8.066 cm^{-1}). While this is a range also observed using Fourier transform infrared or Raman spectroscopy, INS has the advantage that, in the case of confined water, the normal selection rules governing the interaction of light radiation with matter are broken due to local structure disorder, making analysis of spectral intensities difficult. Instead, comprehensive, quantitative, and direct information on the vibrational spectrum can be obtained by INS, where the measured dynamical structure factor is directly related to the density of vibrational states weighted by the squared amplitudes of the atomic oscillations. In other words, INS can measure quantitatively the density of the vibrational states for all possible translational, librational, and intramolecular excitations of confined water, limited only by the frequency-dependent resolution of a given instrumental configuration. Therefore, INS has been used for a variety of studies of water-containing inorganic materials [1,33–36].

Quasielastic neutron scattering is a technique of choice for investigating the mobility of confined water because it investigates translational motions on the 1–1000 ps (10^{-9}–10^{-12} s) time scale, which are common in such circumstances. Because of its utility for analysis of the dynamics of water, QENS has been used to analyze a great variety of both organic and inorganic water-containing materials [3,4,6,12–17,37–54].

To gain further insight into the behavior of such tightly bound water molecules dielectric spectroscopy has also been employed in this study. The dielectric permittivity $\varepsilon^*(\omega) = \varepsilon'(\omega) - i\varepsilon''(\omega)$ can be investigated over a broad frequency spectrum (10^{-1}–10^{6} Hz, or 10–10^{-6} s in this study) and temperature range, allowing it to probe a wide variety of dipolar motions and reorientations. The imaginary component $\varepsilon''(\omega)$ is referred to as the dielectric loss and is proportional to the work done by the electric field to reorientate the dipoles present. The real component $\varepsilon'(\omega)$, known as the dielectric

relaxation, is linked to the imaginary losses by the Kramers-Kronig relationship. Dielectric spectroscopy is particularly suited to analysis of samples such as that examined here, in which the main contribution to the behavior will come from electrically uncompensated dipoles present in a crystalline background, in this case the water molecule. Whereas QENS is sensitive to the movement of individual protons, dielectric spectroscopy is sensitive to slower collective motions of dipolar entities within the sample [55]. The results obtained are mesoscalar in character and influenced by the nature of the environment in which the dipolar entity relaxes [56]. By measuring the dielectric permittivity along a different axis of the crystal the effect of directed motions should be apparent from the differing spectra obtained parallel to or perpendicular to the channels.

A. Sample preparation and characterization

The samples used for this study were gem-quality single-crystal aquamarines purchased from a supplier of cutting rough for the gem industry. Their provenance is unknown, but they were likely from pegmatites in Pakistan or Afghanistan. These were cut into slabs approximately 0.7 mm thick. Each slab was cut parallel to the c axis of the stone. Although available data suggest that the water in beryl is difficult to remove [28,29,57] and thus may similarly be hard to add, we maximized the likely water content of the channels by hydrothermally treating the samples in a steam environment at 200 °C overnight. For the QENS and INS analysis several of these slabs were aligned with their c axes parallel and wrapped in a flat Al-foil packet. The sample for dielectric spectroscopy was prepared as described below.

The major and minor element composition of the aquamarine sample was analyzed using the Cameca SX-50 electron microprobe in the Department of Earth and Planetary Sciences at the University of Tennessee using wavelength-dispersive mode. The results are given in Table I. Normalizing to eight Si, Al, and Fe cations, calculating the Be content by stoichiometry (assuming a full Be site), and obtaining the weight fraction of water by difference yields a beryl stoichiometry of $Be_3Al_2(Si_{5.96}Al_{0.02}Fe_{0.02})O_{18} \bullet 0.625H_2O$. The slight lack of charge balance in this formula is probably due to analytical error. The analysis indicates that this is a low-alkali-metal beryl and thus the water in it is expected to be of type I.

TABLE I. Aquamarine analysis.

Oxide	Weight (%)	Normalized moles
SiO_2	65.2	5.96
Al_2O_3	18.7	2.02
FeO	0.26	0.02
Na_2O	0.14	0.01
CaO	<0.01	
K_2O	<0.01	
BeO[a]	13.65	3.00
H_2O[b]	2.05	0.625
sum	100.00	

[a]By stoichiometry.
[b]By difference.

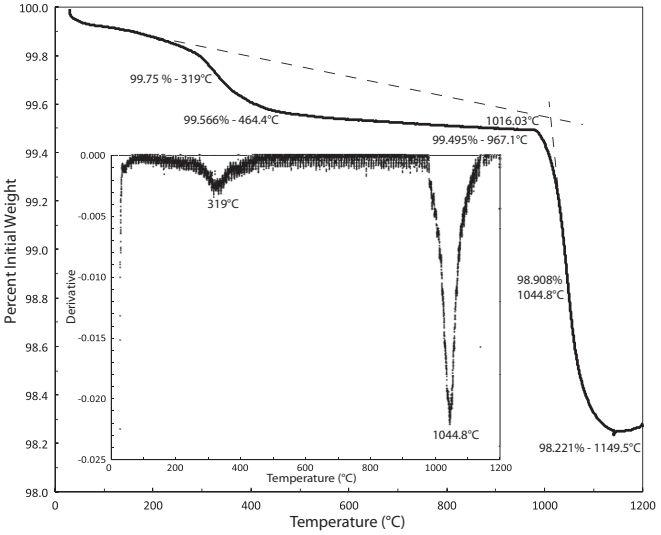

FIG. 2. Thermogravimetric analysis of a sample of the beryl analyzed in this study.

As calculating the water content by difference, as was done in Table I, is relatively inaccurate, we also analyzed the water content of our samples by thermogravimetry. Thermogravimetry analysis was run on a 33.462 mg plate of beryl heated at 10 °C per minute from room temperature to 1200 °C using a TA Instruments Q5000 instrument. The results of this analysis are shown in Fig. 2. The sample lost weight in two steps, an initial weight loss of 0.434 wt.% beginning just above room temperature and peaking at approximately 300 °C and a second at approximately 1016 °C of 1.345 wt.%. The total water loss of 1.779 wt.% is slightly less than that obtained above by difference from the electron microprobe analysis, but the difference is well within the expected uncertainty of the estimation and would suggest a stoichiometry of $Be_3Al_2(Si_{5.96}Al_{0.02}Fe_{0.02})O_{18} \bullet 0.542H_2O$. As there was little surface area to the plate the lower temperature loss is likely too large to be accounted for simply by surface sorption, suggesting there may be two forms of water present in the sample, possibly resulting from the hydrothermal treatment.

IV. EXPERIMENTAL APPROACHES

A. Inelastic neutron scattering

Inelastic neutron scattering experiments were performed using the fine-resolution Fermi chopper spectrometer SEQUOIA at the Spallation Neutron Source at the Oak Ridge National Laboratory (ORNL) [58]. Measurements were made at two incident neutron energies $E_i = 250$ and 800 meV, selected by the Fermi chopper rotating at 480 and 600 Hz, respectively. The former provided good quality spectra at energy losses in the range 50 meV $< E <$ 240 meV and the latter in the range 240 meV $< E <$ 750 meV, with energy resolution being about 2–4% of E_i. The data were recorded over a wide range of scattering angles, from $-30°$ to $60°$ in the horizontal plane and $\pm 18°$ in the vertical direction. Samples

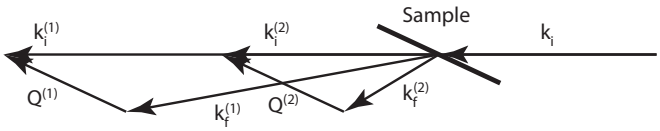

FIG. 3. Scattering geometry of the INS experiment (view from the top). The incident neutrons of selected energy (momentum k_i) enter from right to left. The neutrons are detected simultaneously at various scattering angles determined by the geometry of the detectors in the spectrometer. The scattered neutrons change their direction and energy and hence the absolute value of their momentum k_f. The spectra presented in Figs. 5 and 6 were obtained by combining only those detectors for which the momentum transfer Q for energies transfers around 450 and 200 meV were almost parallel to the sample surface in the equatorial scattering plane, respectively. The c axis of the crystals was in the sample plane and was oriented either in the equatorial scattering plane resulting in momentum transfer being parallel to the c axis for the energy transfers around 450 and 200 meV for $E_i = 800$ and 250 meV, respectively, or vertical, which was perpendicular to all Q directions for scattering in the equatorial plane.

in the shape of rectangular slabs (six pieces of varying sizes ~0.7 mm thick) were mounted in a vacuum-sealed thin-walled flat aluminum container, which was mounted on the cold head of a closed-cycle refrigerator. Measurements were performed at $T = 7$ K to reduce temperature effects (Debye-Waller factor and multiphonon neutron scattering). Inelastic neutron scattering measurements were made with the sample in two different orientations, one with $\mathbf{Q}$ perpendicular to the c axis (the c axis was vertical) and the other with $\mathbf{Q}$ parallel to the c axis (the c axis was horizontal). The scattering geometry is illustrated in Fig. 3. In both orientations the sample was placed so as to have a 65° angle between the incoming neutron beam and the normal to the sample plates. For the c axis oriented horizontally this resulted in the Q vector being almost parallel to the c axis for a neutron energy loss of $E = 450$ meV at $E_i = 800$ meV and a scattering angle of ~15° (with maximum ±10° deviation for other scattering angles between 8° and 25°). The same was true for $E = 200$ meV at $E_i = 250$ meV and a scattering angle of ~45° (with deviation from − 10° to 2° for scattering angles between 15° and 60°). The collected neutron scattering data were transformed from time-of-flight and instrument coordinates to the dynamical structure factor $S(Q,E)$ using a standard program mantidplot (see [59]) for INS data reduction at direct geometry spectrometers and then to a generalized vibrational density of states $G(E) = S(Q,E)E/\{Q^2[n(E,T)+1]\}$, where $n(E,T) = 1/[\exp(E/k_BT) - 1]$ is the population Bose factor. The sample in each orientation occupied essentially the same space in the beam and had the same width, height, thickness, and angle between the sample surface and the neutron beam direction. Thus all sample geometrical factors were almost identical for analyses carried out with the c axis parallel and perpendicular to the momentum transfer. This permits the two sets of measured INS spectra to be compared directly. Observed differences in the features of the two spectra are therefore entirely due to the changes in the water vibrational properties along and perpendicular to the c axis.

B. Quasielastic neutron scattering

The quasielastic neutron scattering experiment was carried out on BASIS, a backscattering spectrometer at the Spallation Neutron Source, ORNL [60]. In a general (that is, not necessarily quasielastic) inelastic neutron scattering experiment, the scattering intensity is measured as a function of the neutron energy transfer $E = E_i - E_f$, and the scattering momentum transfer $\mathbf{Q} = \mathbf{k}_i - \mathbf{k}_f$, where the indices i and f stand for the initial and the final state of the incident neutron. The direction of the scattering momentum transfer is defined by the initial and the final neutron momentum $\mathbf{k}$ and its magnitude depends on the scattering angle 2θ as $Q = (k_i^2 + k_f^2 - 2k_ik_f\cos2\theta)^{1/2}$. For small energy transfers in the quasielastic regime, which is a special case of inelastic scattering, where the magnitude (but not necessarily the direction) of $\mathbf{k}$ changes only slightly, the following approximation is often used: $Q = 2k\sin(2\theta/2)$. The scattering angles (thus the $\mathbf{Q}$ values and directions in the quasielastic regime) on a neutron time-of-flight spectrometer such as BASIS are permanently fixed by the positions of the crystal analyzers and detectors. Therefore, different orientations of the aligned channels in the sample with respect to the fixed directions of various $\mathbf{Q}$ can be achieved by rotating or otherwise changing the orientation of the sample. The scattering geometry presented in Fig. 4 shows that, for each measurement, the sample was oriented so that the channels were either parallel to a selected $\mathbf{Q}$ direction (for instance, $\mathbf{Q} = 0.5$ Å^{-1} as shown in Fig. 4), allowing us to measure motions along the channels for that Q orientation, or simultaneously perpendicular to all $\mathbf{Q}$ directions (out-of-plane channel orientation in Fig. 4), allowing us to measure motions perpendicular to the channels for all $\mathbf{Q}$ directions. For the Q-parallel orientations the scattering patterns at all values of $\mathbf{Q}$ are measured simultaneously at each sample orientation, but the channels are parallel to $\mathbf{Q}$ only for a single scattering angle (that is, $\mathbf{Q}$ value) at a time. For the Q-perpendicular orientation, the scattering patterns at all values of $\mathbf{Q}$ are again measured simultaneously, but the channels are simultaneously perpendicular to all $\mathbf{Q}$ directions. The Q-perpendicular orientation in Fig. 4 displays, strictly speaking, only one channel. For the real single-crystal sample in the shape of a thin plate, the orientation of the plate with respect to the incident beam can be varied arbitrarily by rotation of the sample about the vertical axis; this would not affect the scattering geometry in the Q-perpendicular orientation, except for the effect of the different neutron absorption in the sample as a function of scattering angle. For the Q-perpendicular orientation, we intentionally chose to orient the sample at 135° with respect to the incident beam. This means that all the scattering patterns that we analyzed up to the largest value of 1.1 Å^{-1} were measured in transmission geometry, whether in the Q-perpendicular or the Q-parallel orientation, thereby eliminating possible systematic differences between scattering geometries.

A closed-cycle refrigerator controlled the temperature of the sample. For the resolution function, which was specific to each sample orientation, data measured at a baseline temperature of 5 K were used. The measurements of the confined water dynamics have been carried out at temperatures of 300 and 370 K. At each Q, the data were fitted using the

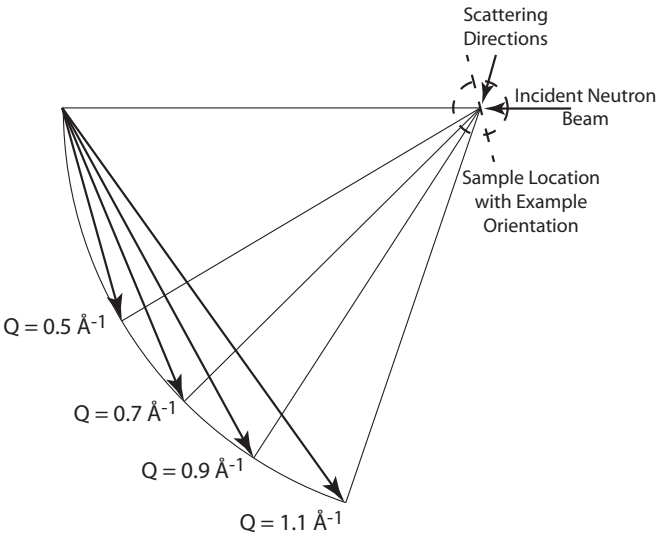

FIG. 4. Scattering geometry of the QENS experiment (view from the top). The incident neutrons enter from right to left. The neutrons are detected simultaneously at various, but fixed, scattering angles determined by the geometry of the analyzers and detectors in the spectrometer. The direction of the scattered neutrons changes significantly, but the absolute value of their momentum changes only slightly and the end points of the initial and the final neutron momentum lie on a circle (solid line). The final scattering momentum (radial solid lines) and momentum transfer $-\mathbf{Q}$ (chordal solid lines) are shown for the Q values 0.5, 0.7, 0.9, and 1.1 Å^{-1} used in the data analysis. The channels in the sample can be oriented either parallel to a particular Q direction (one at a time, e.g., for $Q = 0.5\ \text{Å}^{-1}$, as shown in the figure by a dashed line passing through the origin, a Q-parallel orientation in our notation) or perpendicular to all Q directions at once when the channels are in the out-of-plane direction, as shown by a dashed circle centered at the origin (a Q-perpendicular orientation in our notation).

following expression:

$$I(E,Q) = \{x(Q)\delta(E) + [1 - x(Q)]S(E,Q)\} \otimes R(E,Q) + [B_1(Q)E + B_2(Q)], \quad (1)$$

where the $x(Q)$ is the relative spectral weight of the elastic scattering signal described by the delta function $\delta(E)$ centered at zero energy transfer, $R(E,Q)$ is the resolution function, $B_1(Q)E + B_2(Q)$ is a linear background term, and $S(E,Q)$ is the model scattering function that describes the physics of the quasielastic scattering process.

For mobile molecules confined in narrow channels parallel to the **Q** direction (as opposed to the more common samples with randomly oriented channels), the scattering function can either be a simple Lorentzian

$$S(E,Q) = \frac{1}{\pi}\frac{\Gamma(Q)}{E^2 + \Gamma(Q)^2} \quad (2)$$

for a normal diffusion process or assume a more complex spectral shape for a single-file diffusion process, when the diffusing molecules cannot pass one another:

$$S(E,Q) = \frac{y}{E}g(y), \quad (3)$$

where $y = G(Q)/(2\pi E)^{1/2}$ and $g(y)$ is a Fresnel integral-based function for which there exists a rational approximation [61] that we used in our fits. It should be noted that in the original paper discussing these scattering functions [61] an unrestricted diffusion model (as either normal or single-file diffusion) was specifically assumed, for which $\Gamma(Q) = DQ^2$ and $G(Q) = FQ^2/(2\pi E)^{1/2}$, where D and F are the diffusion coefficients for the normal and single-file diffusion processes, respectively. However, we choose to perform fits at each Q value with either Eqs. (1) and (2) or Eqs. (1) and (3), compare the agreement of the fits with the data, and see whether the so obtained $\Gamma(Q)$ or $G(Q)$ follow any particular dependence on the Q, rather than to fix the Q^2 dependence for D and F. Initially, our main reason for using empirically fitted $\Gamma(Q)$ or $G(Q)$ was to allow for the analysis in the Q-parallel geometry of the data (which are collected simultaneously) at Q values where the direction of **Q** is not necessarily parallel to the channels. However, in the process of data analysis we realized that the Q dependence of the broadening of the model scattering function was completely different from the Q^2-proportional law expected in the diffusion regime. This is likely because of the extreme confinement experienced by the water molecules, which provided additional justification for our use of empirically fitted $\Gamma(Q)$ and $G(Q)$ equations.

C. Dielectric spectroscopy

Dielectric spectroscopy measurements were carried out using a Novocontrol BDS 80 cryogenic dielectric spectrometer, based on an Alpha analyzer [62]. The accuracy of the measurement in terms of $\tan(\delta)$ is less than 10^{-4}. The frequency range was 0.1 Hz to 1 MHz and the temperature range was set from $-40\ ^\circ\text{C}$ to $90\ ^\circ\text{C}$ with intervals of $10\ ^\circ\text{C}$. Two samples were cut from a single crystal. One crystal (5.5 mm long, 0.5 mm thick, and 1.5 mm wide) was polished perpendicular to the c crystallographic axis (equivalent to the Q-parallel orientation for INS and QENS) and gold electrodes were deposited on it by sputtering. The other was polished perpendicular to the a axis of the crystal (equivalent to the Q-perpendicular orientation for INS and QENS) with a 6 mm length, 0.5 mm thickness, and 6.0 mm width and had aluminum electrodes deposited on it using a chemical vapor deposition process.

The basics of dielectric spectroscopy are well established [55]. In the frequency range measured the dielectric permittivity $\varepsilon^*(\omega)$ can be calculated from the measured complex impedance of the sample by

$$\varepsilon^*(\omega) = \frac{1}{i\omega C_0 Z(\omega)}, \quad (4)$$

where ω is the cyclic frequency, i is the root of -1, C_0 is the geometric capacitance of the sample, and $Z(\omega)$ is the measured complex impedance of the sample [55,56]. Implicit in the technique is that the measurement is carried out in the direction of the probing field. For anisotropic samples this means that the dielectric permittivity will likewise depend on the sample orientation.

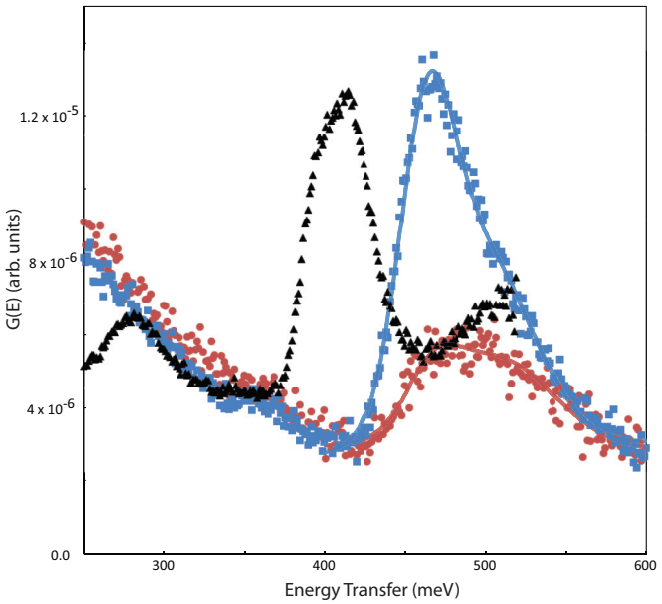

FIG. 5. (Color) The INS spectra of beryl measured with the direction of Q either parallel to the c axis (blue squares) or perpendicular to the c axis (red circles) for E_i = 800 meV. Data for ice Ih [63] are shown for comparison (black triangles).

V. RESULTS AND DISCUSSION

A. Inelastic neutron scattering

Figure 5 shows the INS spectra for two sample orientations, Q parallel and Q perpendicular to the c axis for an incident energy of 800 meV. The intensity of the peaks in INS spectra in a one-phonon approximation can be expressed as

$$S^{\mathrm{inc}}_{1\mathrm{ph}}(\mathbf{Q},E) = \sum_i \frac{\sigma_i \hbar^2}{6\mathrm{NEM}_i} \exp[-(\mathbf{Q}\mathbf{u}_i)^2][n_B(E,T)+1] \times \sum_{j,\mathbf{q}} |\mathbf{Q}\mathbf{e}_i(j,\mathbf{q})|^2, \quad (5)$$

$$(\mathbf{Q}\mathbf{u}_i)^2 = \int \sum_{j,\mathbf{q}} \frac{\hbar^2}{6\mathrm{NEM}_i} |\mathbf{Q}\mathbf{e}_i(j,\mathbf{q})|^2 [2n_B(E,T)+1] \times \delta[E - E(j,\mathbf{q})]dE, \quad (6)$$

where σ_i and M_i are neutron scattering cross section and mass of atom i, $E(j,\mathbf{Q})$ and $\mathbf{e}_i(j,\mathbf{Q})$ are the phonon eigenvalues and eigenvectors (for atom i) for the phonon mode j at $\mathbf{Q}$ point in the Brillouin zone, $n_B(E,T)$ is the phonon population Bose factor, and $\mathbf{u}_i$ is a vector of atom i displacement due to all phonon modes. The ratio σ_i/M_i for hydrogen atoms is at least 100 times larger than that of other atoms in the beryl, so we can assume that the peaks observed in the INS spectra are all related to the neutron scattering from hydrogen atoms. As dry beryl should not have any vibrations at energies above 200 meV (and surely none around 450 meV) all the spectral features in that energy range are clearly due to neutron scattering from water protons.

For the high incident neutron energy data set (Fig. 5), the O-H stretching mode peaks above 400 meV can be fitted by a sloped linear background and two Gaussian functions positioned at ∼465 and ∼500 meV, respectively, as

$$G(E) = a + bE + c\exp\{-[(E-d)/f]^2\} + g\exp\{-[(E-h)/k]^2\}, \quad (7)$$

where d, f, h, and k are in meV and the fit parameters are $a = 3.18 \times 10^{-6}$, $b = -5.59 \times 10^{-10}$, $c = 2.45 \times 10^{-6}$, $d = 507$, $f = 49.6$, $g = 1.34 \times 10^{-6}$, $h = 467$, and $k = 23.8$ for the Q-perpendicular orientation and $a = 2.05 \times 10^{-6}$, $b = 1.66 \times 10^{-9}$, $c = 5.38 \times 10^{-6}$, $d = 496$, $f = 45.9$, $g = 6.99 \times 10^{-6}$, $h = 463$, and $k = 23.7$ for the Q-parallel orientation. As can be seen in Fig. 5, the positions of both Gaussian functions are significantly higher than those observed in ice Ih or any other known ice phases [64]. However, the position of the first Gaussian (∼465 meV) almost coincides with the values of the intramolecular O-H stretching modes for a free water molecule, which are 454 and 466 meV for the symmetrical and asymmetrical vibrations, respectively [65,66]. The second (broad) component can be explained as a multiphonon neutron scattering, mainly a combination of the optic mode at ∼465 meV and an intermolecular low-energy band centered at ∼35 meV. The coincidence of the peak at ∼465 meV with that of free water rather than ice suggests that there are no hydrogen bonds acting on this water molecule.

The intensity of the component at ∼465 meV for the Q-parallel orientation is about 5.375 times larger than that for Q perpendicular to the c axis. If we assume that the H—H bond for water in beryl is oriented along the c axis (type-I water), as would be expected for a low-alkali-metal beryl, and the H—O—H angle for water is about ∼106°, then the intensity for the Q-parallel-to-c orientation will be proportional to $\sin(106^\circ/2)^2 = 0.64$ and for Q perpendicular to the c axis with the c axis oriented vertically it should be proportional to $\cos(106^\circ/2)^2\langle\cos(\phi)^2\rangle$, where ϕ is an angle between the projection of the O—H bond on the horizontal plane and the Q vector. If we assume that ϕ is randomly oriented, that is, that the H—O—H plane for any given water molecule is randomly oriented about the c axis, then the averaged value of $\langle\cos(\phi)^2\rangle = 0.5$. In this case the intensity of the peak in the Q-perpendicular direction will be ∼0.18. Thus the estimated ratio of the peak intensities in two orientations should be ∼3.56, which is smaller (by a factor 1.5) than the experimental value of 5.375.

The intensity of the peak is, however, also affected by the Debye-Waller factor $\exp[-(\mathbf{Q}\mathbf{u}_i)^2]$ [see Eq. (5)]. Given the hexagonal symmetry of beryl, it is likely that the Debye-Waller factors for water perpendicular and parallel to the c axis are anisotropic. (In their neutron diffraction study of beryl Artioli *et al.* [29] only refined isotropic temperature factors for water in the channels.) That is, the mean-square displacements $\langle u^2\rangle$ for water protons parallel and perpendicular to the c axis are different. If we assume that the estimated intensity deficit (1.5 times) is completely due to the anisotropy of the Debye-Waller factor, then $\exp[-(u^2_{\mathrm{par}} - u^2_{\mathrm{perp}})Q^2] = 1.5$ and therefore $u^2_{\mathrm{par}} - u^2_{\mathrm{perp}} = -0.006$ Å^2. That is, the data suggest that the mean-square displacement perpendicular to the c axis is larger than that parallel to it.

The spectra for the Q-parallel and Q-perpendicular orientations measured with $E_i = 250$ meV are shown in Fig. 6. There

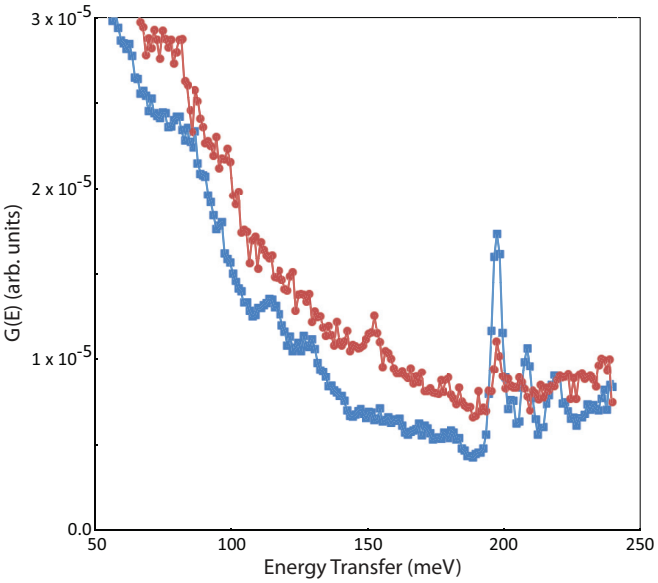

FIG. 6. (Color) The INS spectra of beryl measured with the direction of Q either parallel to the c axis (blue squares) or perpendicular to the c axis (red circles) for $E_i = 250$ meV.

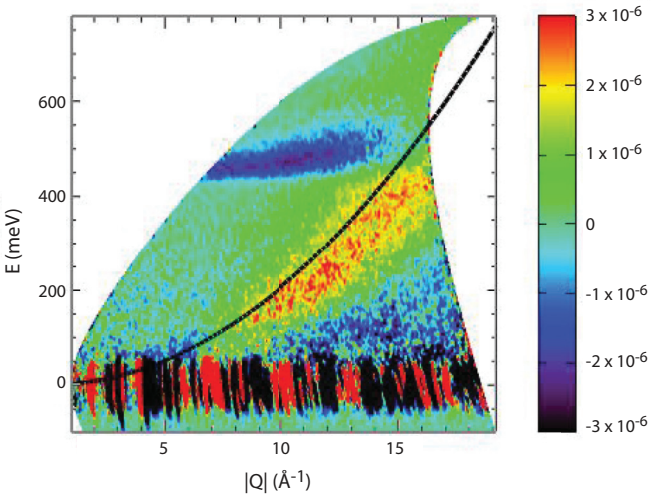

FIG. 7. (Color) Differences between the intensity of the INS spectra for the Q-perpendicular and Q-parallel orientations as a function of Q and E for $E_i = 800$ meV. The black curve shows the dependence of neutron recoil scattering on free protons.

are three strong peaks for the Q-parallel-to-c orientation at $E =$ 197.5, 208.5, and 219 meV and three smaller peaks at ∼86, 114, and 128 meV. For the Q-perpendicular-to-c orientation only two peaks were observed, one at ∼152 meV and another one at 197.5 meV. Only a peak at 197.5 meV occurs at the same energy for both sample orientations. There is a peak due to intramolecular H—O—H bending at 200–206 meV in the vibrational spectra of water and ice [64]: the so-called water scissors mode. It is typically relatively broad in these spectra. In the Q-parallel spectrum (Fig. 6) this has split into three strong, relatively narrow peaks. This indicates that water molecules in beryl are strongly bound in the directions perpendicular to the water O—H bonds and cannot vibrate freely, but more weakly bound parallel to the bond, and sit in three nonsymmetrically equivalent positions.

The three week peaks in the Q-parallel orientation at ∼86, 114, and 128 meV are somewhat more difficult to explain. This is the region of the spectrum, between approximately 50 and 120 meV, in which librational modes are expected to occur. However, the lowest energy of these peaks occurs at a significantly higher energy than the lowest peaks recorded for ices [64]. Alternatively, these may correspond to vibrations of water coupled to vibrations of the beryl lattice itself. No peaks are observed in this region in the Q-perpendicular orientation, suggesting that they are either absent or so spread out in energy as to be unobservable.

In addition to changes in the number and intensity of peaks between the two spectra, the intensity of the baseline of the spectrum in the range 50–240 meV for the spectrum in the Q-perpendicular-to-c (c axis vertical) orientation is higher than for the Q-parallel-to-c (c axis horizontal) orientation. This is probably due to a greater intensity of the low-energy modes of water molecules in the direction perpendicular to the c axis, which produces the larger $\langle u^2_{\text{perp}} \rangle$ values and as a result a larger multiphonon contribution at higher energies. This conclusion is in agreement with the optical spectroscopic measurements [67], where they also observe large translational or librational vibrations in the direction perpendicular to the c axis.

For a single harmonic oscillator of mass m with ground state energy $\hbar\omega_0/2$ the intensity of the neutron scattering due to a transition of the oscillator from the ground state to the nth excited state can be expressed as

$$S_n(Q,\omega) = \frac{1}{n!}\left(\frac{\hbar Q^2}{2m\omega_0}\right)^n \exp\left(\frac{-\hbar Q^2}{2m\omega_0}\right)\delta(\hbar\omega - n\hbar\omega_0). \quad (8)$$

It can be shown that the maximum of this intensity as a function of Q follows the dependence $n\hbar\omega_0 = \hbar^2 Q^2/2m$, which is the same expression as for the recoil dependence of neutron scattering of free particle of mass m in impulse approximation (for large momentum transfer), $E_R = \hbar^2 Q^2/2m$ [68].

Figure 7 shows a contour plot of the difference in intensity as a function of energy and Q between the two orientations of the beryl crystal. These data show that there is an increased intensity in the Q range larger than 10 Å^{-1} at energy transfers between 150 and 400 meV for the c-axis vertical orientation. The recoil line for neutron scattering from a free proton is also shown. The observed extra intensity in the Q-perpendicular orientation closely approximates the recoil line. This indicates a softer "effective" potential experienced and thus greater ease of motion by water protons in the direction perpendicular to the c axis. The deviation from the ideal recoil line is probably due to limited values of momentum transfer, anharmonicity, and involvement of many low-energy modes in the process (it is not a single harmonic oscillator). Due to the softer effective potential in the direction perpendicular to c axis the corresponding $\langle u^2_H \rangle$ should be larger and the Debye-Waller factor $\exp(-\langle u^2_H \rangle Q^2)$ for large Q should be smaller, thus the stretching modes near 500 meV in that direction are strongly suppressed.

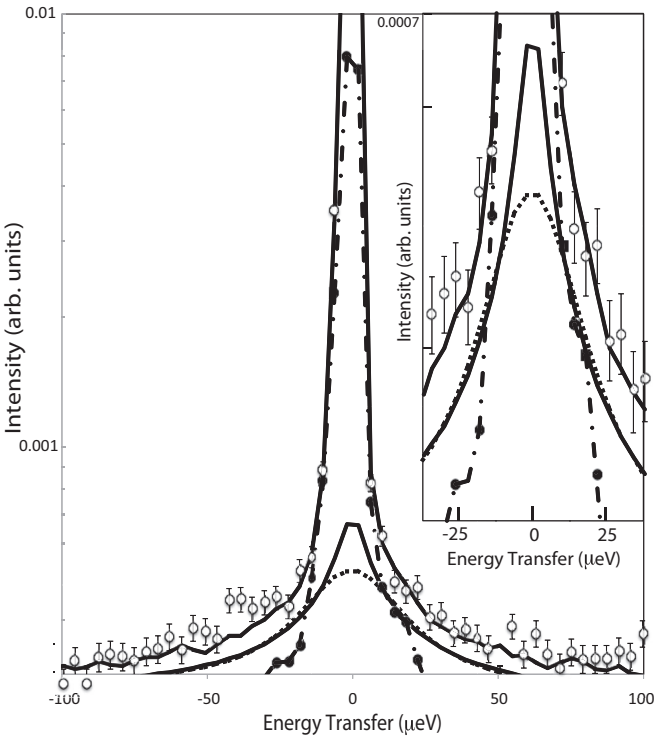

FIG. 8. Data (open symbols) and fits (lines) at $Q = 1.1$ Å^{-1} obtained at 370 K with the sample channels oriented parallel to $Q = 1.1$ Å^{-1}. Dashed lines show the overall data fit and the quasielastic component obtained using Eqs. (1) and (2) for regular diffusion. Solid lines show the overall data fit and the quasielastic component obtained using Eqs. (1) and (3) for single-file diffusion. Closed symbols connected by the dash-dotted line show the resolution function. For clarity, the data were rebinned to 4 μeV and the elastic line intensity was truncated. The inset shows the central part of the data set.

B. Quasielastic neutron scattering

A representative example of the QENS data at $Q = 1.1$ Å^{-1} measured at 370 K with the sample channels oriented parallel to $\mathbf{Q} = 1.1$ Å^{-1} is shown in Fig. 8. The overall fits using Eqs. (1) and (2) for regular diffusion and Eqs. (1)–(3) for single-file diffusion look very similar because of the strong elastic component, the relative strength of which is also model dependent. However, the respective quasielastic components are quite different. The single-file diffusion model yields a more peaked (even after convolution with the resolution function) quasielastic component. The strong elastic component is an unavoidable consequence of scattering from the matrix, as well as from water molecules or hydroxyl groups (not present in beryl) that are immobile on the time scale of the measurement. Such immobile water molecules in hydrated matrices often render direct subtraction of the signal from the "dry" sample not particularly useful. This is because the elastic signal for a fully dried sample, while still large, will not include the signal from the immobile waters. Thus the elastic signal still needs to be treated as an adjustable parameter.

Comparison of the fit agreement factors (Table II) demonstrated that the single-file diffusion model yields better agreement for the Q-parallel sample orientations, whereas the regular diffusion model better describes the data for the Q-perpendicular sample orientation. The trend is rather systematic, as there are only two outliers out of 28 pairs of agreement factors, excepting a few points where the agreement factors are the same for both models. We therefore conclude that the water molecules undergo regular diffusionlike motions in directions perpendicular to the channels axes, whereas along the axes their mobility is better described as single-file diffusion.

Figures 9 and 10 show the quasielastic broadening parameters $\Gamma(Q)$ from Eq. (2) for the regular diffusion model and $G(Q)$ from Eq. (3) for the single-file diffusion model at 370 and 300 K, respectively. The corresponding values of the elastic scattering fraction, $x(Q)$ from Eq. (1), are shown in Fig. 11. As the Q dependence of the two models is very similar, it is obvious that fits with either the regular or single-file diffusion model describe, albeit in somewhat different terms, the same water motions. The choice of the best model therefore needs to be based on the best fits summarized in Table II.

Several conclusions can be reached from the temperature and Q dependence of the quasielastic fit parameters. Most of the scattering signal is elastic and originates from the matrix and water molecules that are immobile on the time scale of the measurement. However, the dynamics of the mobile water molecules appears to be predominantly translational, although the influence of confinement is strong. This is evident from the Q-dependent quasielastic broadening presented in Figs. 9 and 10, which tends to increase with Q and is reminiscent of jump diffusion models with either a fixed jump length or a distribution of jump lengths [69]. This conclusion is supported by the $x(Q)$ data (Fig. 11), whose Q dependence is much weaker than would be expected for highly localized rotational motions, although the slow decay of $x(Q)$ is consistent with some degree of spatial confinement in the matrix for translation motions because it implies a

TABLE II. Agreement factor $\chi^2 = \Sigma(I_{\text{expt}} - I_{\text{mod}})^2/(N_{\text{obs}} - N_{\text{param}})$ obtained from the fits using the regular diffusion and single-file diffusion models. For each Q value, the lower values, indicating better agreement, are shown in bold.

	Regular diffusion [Eqs. (1) and (2)]				Single-file diffusion [Eqs. (1) and (3)]			
	0.5 Å^{-1}	0.7 Å^{-1}	0.9 Å^{-1}	1.1 Å^{-1}	0.5 Å^{-1}	0.7 Å^{-1}	0.9 Å^{-1}	1.1 Å^{-1}
370 K, $Q = 0.7$ Å^{-1} parallel to channels	**1.358**	**1.373**	1.525	1.171	1.361	1.383	**1.513**	**1.154**
370 K, $Q = 0.9$ Å^{-1} parallel to channels	1.335	**1.212**	1.143	1.253	**1.313**	**1.212**	**1.142**	**1.227**
370 K, $Q = 1.1$ Å^{-1} parallel to channels	1.360	1.437	1.270	1.062	**1.345**	**1.424**	**1.253**	**1.046**
370 K, all Q perpendicular to channels	**1.528**	**1.413**	**1.398**	**1.261**	1.530	1.441	1.400	1.262
300 K, $Q = 0.5$ Å^{-1} parallel to channels	1.302	**1.176**	1.160	1.258	**1.301**	**1.176**	**1.152**	**1.256**
300 K, $Q = 1.1$ Å^{-1} parallel to channels	1.389	1.306	1.234	1.487	**1.386**	**1.295**	**1.218**	**1.426**
300 K, all Q perpendicular to channels	**1.897**	**1.539**	**1.414**	**1.254**	1.905	1.547	1.437	1.264

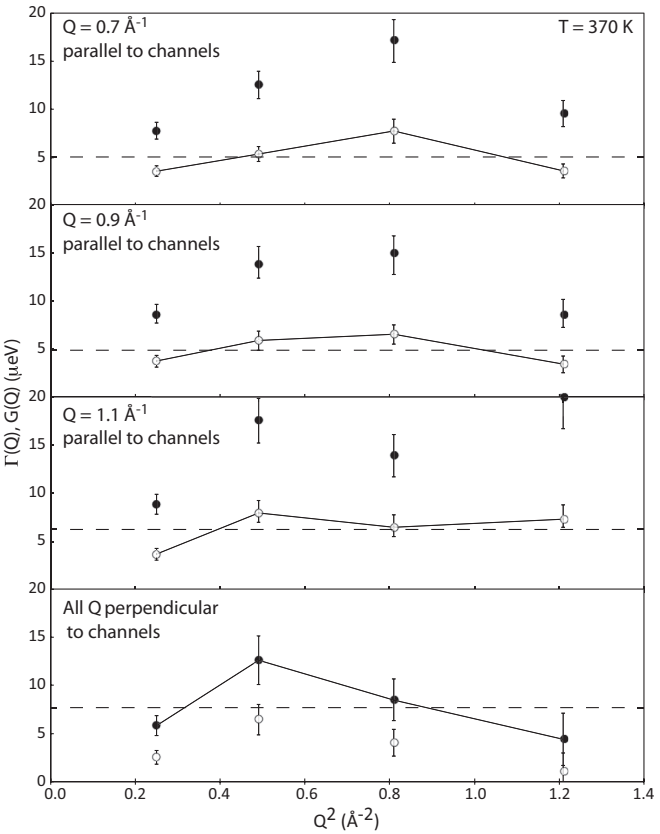

FIG. 9. Broadening of the model scattering function measured at 370 K. Closed symbols denote the parameters $\Gamma(Q)$ obtained from fits with the regular diffusion model (1) and (2). Open symbols denote the parameters $G(Q)$ obtained from fits with the single-file diffusion model (1) and (3). The horizontal dashed line indicates the Q-averaged value of the broadening for the model that shows the better agreement with the data (that is, the regular diffusion model for the Q-perpendicular orientations and the single-file diffusion for the Q-parallel orientations; see Table II).

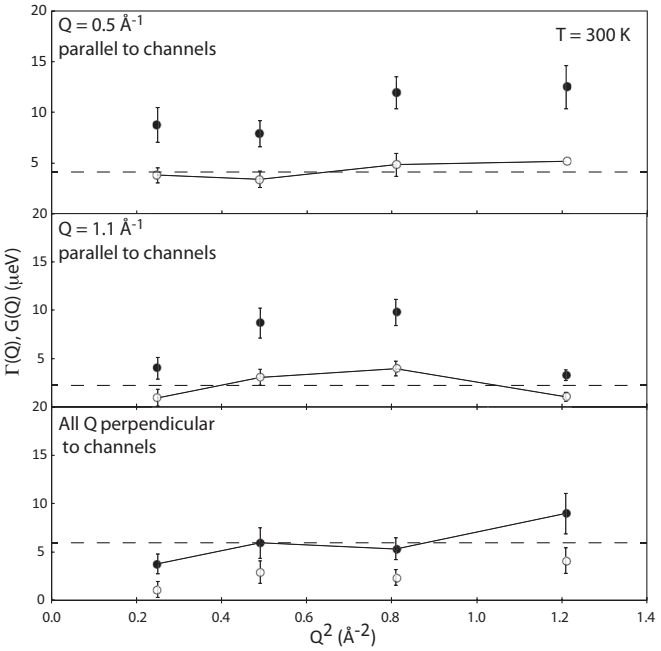

FIG. 10. Broadening of the model scattering function measured at 300 K. Closed symbols denote the parameters $\Gamma(Q)$ obtained from fits with the regular diffusion model (1) and (2). Open symbols denote the parameters $G(Q)$ obtained from fits with the single-file diffusion model (1) and (3). The horizontal dashed line indicates the Q-averaged value of the broadening for the model that shows the better agreement with the data (that is, the regular diffusion model for the Q-perpendicular orientations and the single-file diffusion for the Q-parallel orientations; see Table II).

relatively large localization radius [70]. Indeed, the expected contribution from highly localized rotational motions can often be neglected at Q values below 1 Å^{-1} [70]. Despite the translational character of the dynamics observed, averaging over the moderately-Q-dependent quasielastic broadening yields a meaningful characteristic relaxation (diffusion) time τ as $\hbar/\Gamma$, where $\hbar$ is the reduced Planck constant. Interestingly, and counterintuitively, confinement effects are more pronounced for diffusion along the channels, as evidenced by the somewhat stronger Q dependence of $x(Q)$ in this direction (Fig. 11), which is also consistent with the single-file (as opposed to regular) diffusion process observed in this direction and the somewhat smaller average values of the QENS broadening for the Q-parallel orientations compared to the Q-perpendicular orientation (Figs. 9 and 10). These observations are consistent with the conclusion above from the INS data on the softer effective potential for water protons in the direction perpendicular to the c axis.

The above analysis makes no assumptions about the character of the water dynamics that yields the observed QENS spectra. While the original theoretical paper investigating one-dimensional diffusion by QENS [61] assumed an unrestricted (translational) diffusion model, we did not assume any specific Q dependence of the QENS broadening. That is, we made no *a priori* assumption of either a translational or rotational character of the diffusion of the confined water. Instead, we obtained QENS broadening for each Q value independently and analyzed the results to determine whether its Q dependence is indicative of translational or rotational diffusion. Several arguments support the conclusion that the water dynamics is primarily translational: (i) Quasielastic broadening (Figs. 9 and 10) tends to increase with Q, which would not be the case for purely rotational motions, (ii) the Q dependence of the $x(Q)$ data [elastic scattering contribution (Fig. 11)] is much weaker than would be expected for highly localized rotational motions, and (iii) the expected contribution from highly localized rotational motions can often be neglected at Q values below about 1 Å^{-1} for water in general [70]. Similarly, the μeV dynamics of water in comparably tight confinement in zeolites such as NaA, NaX, and NaY [22,24] was also judged to be of predominantly translational character, although tight confinement suppresses the strong Q dependence of the QENS broadening, especially at lower Q values.

Analysis of the data sets at 370 and 300 K suggests that there is some temperature dependence of the QENS broadening, which decreases as the temperature is decreased, indicating slowing of the water diffusion. Because the beam time required for a more systematic measurement of the full QENS data set as a function of temperature would be prohibitive, we performed an elastic intensity temperature scan. On a

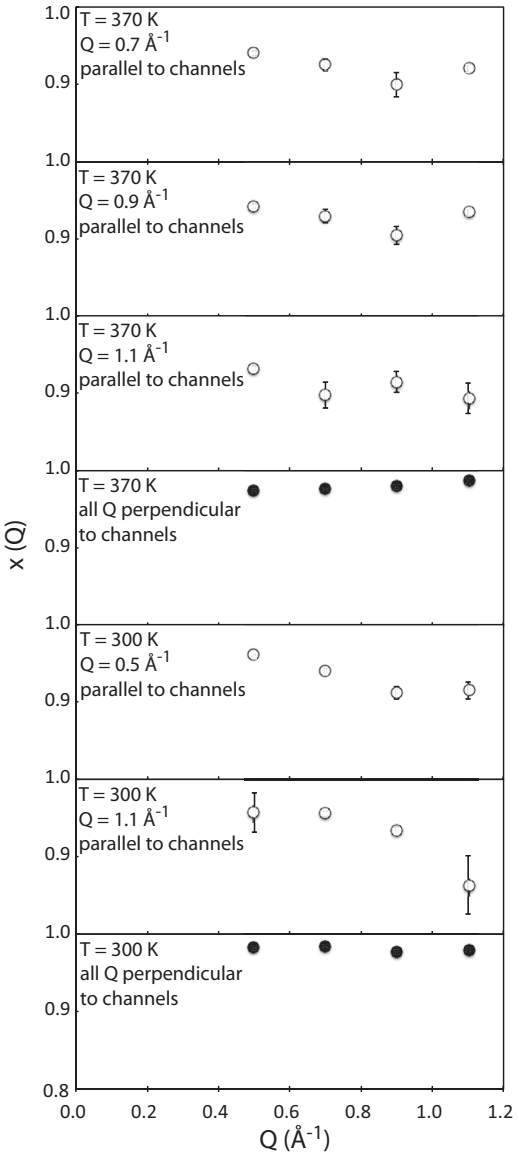

FIG. 11. The Q dependence of the relative spectral weight of the elastic signal [parameter $x(Q)$ in Eq. (1)] obtained using fits with Eqs. (1) and (2) for regular diffusion for the Q-perpendicular orientation (closed symbols) and with Eqs. (1)–(3) for single-file diffusion for the Q-parallel orientations (open symbols).

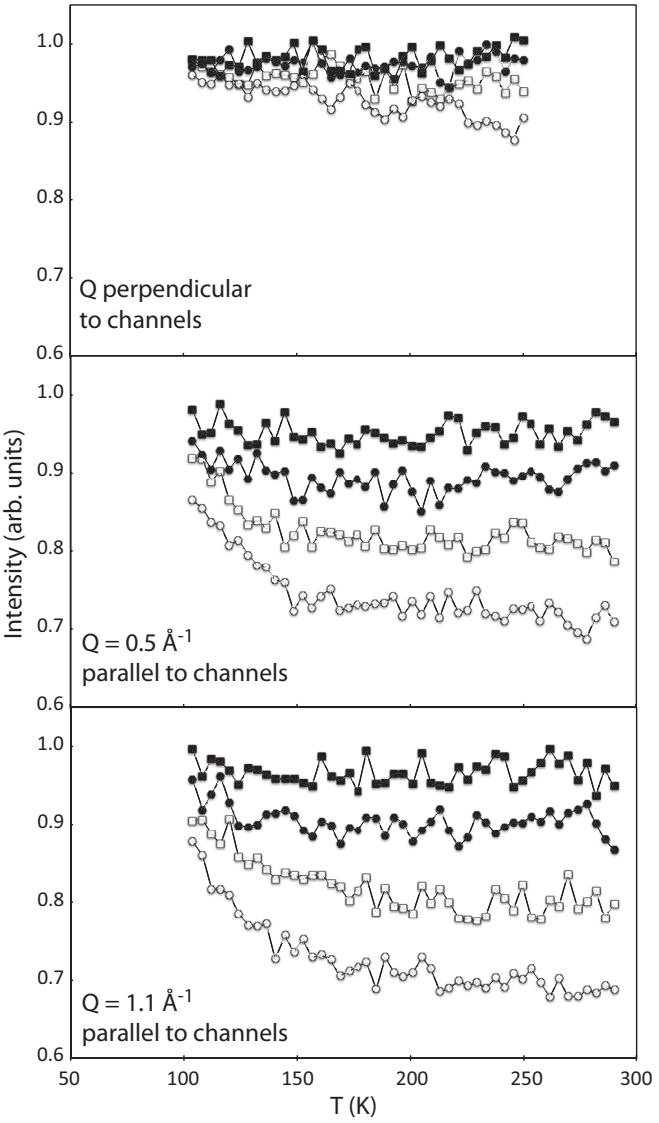

FIG. 12. Temperature dependence of the elastic scattering intensities measured at three different sample orientations for four different scattering angles. Open circles denote $Q = 1.1$ Å^{-1}, open squares $Q = 0.9$ Å^{-1}, closed circles $Q = 0.7$ Å^{-1}, and closed squares $Q = 0.5$ Å^{-1}. Data in the middle and bottom panels are for the sample oriented so that the channels are parallel to the scattering vector whose magnitude is 0.5 A^{-1} (middle panel) or 1.1 A^{-1} (bottom panel). In each of the three sample orientations, as shown in the top, middle, and bottom panels, the data were collected at four Q values (four scattering angles).

time-of-flight backscattering spectrometer such as the BASIS, this technique is implemented by measuring the temperature-dependent spectra for a short time at each temperature and plotting the scattering intensity integrated over the elastic peak as a function of temperature [71]. The results of these measurements are shown in Fig. 12. In the Q-perpendicular orientation, little temperature dependence is observed. In contrast, the data collected using the Q-parallel orientations show a systematic increase in the elastic scattering below approximately 150 K, indicating gradual "freezing out" of the single-file diffusion process along the channels, but no obvious effect on motions perpendicular to the channel direction.

The possibility of single-file diffusion process for confined water has been discussed in a molecular dynamic simulation study of water in silicalite, a hydrophobic all-silica zeolite [72]. In that material confined water appeared to be mostly in the form of amorphous solidlike clusters at temperatures below 225 K. A slow molecule interchange occurring among the clusters gave rise to a single-file-like diffusion. In the present study, the diffusion along the channels appears to remain single-file-like even at 370 K. Possibly this is because the channels in beryl are narrower than those in silicalite [72].

A strong degree of water confinement in beryl is evident from the values of QENS broadening presented in Figs. 9 and 10. The observed half-width at half maximum (HWHM) of several μeV corresponds to relaxation times of several

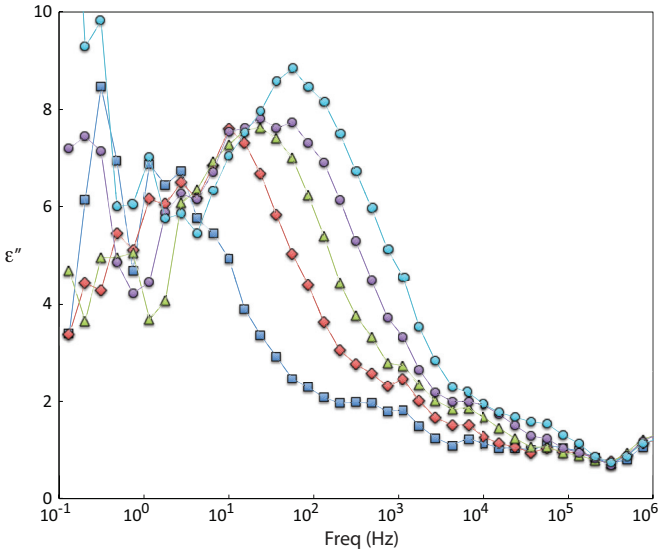

FIG. 13. (Color) Dielectric losses ε'' of a beryl crystal, measured along the a axis. The average dielectric permittivity ε^* of the crystal in this direction is about 10. As can be seen, a weak temperature-activated process is revealed in this direction: 40 °C, blue squares; 10 °C, red diamonds; 20 °C, green triangles; 50 °C, purple circles; and 90 °C, light blue circles.

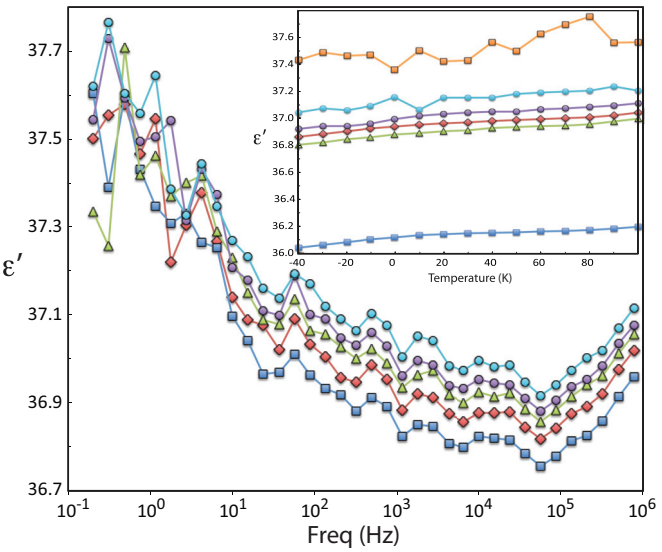

FIG. 14. (Color) Dielectric relaxation of a beryl crystal measured parallel to the c axis. While the tail of a low-frequency process is visible, it does not appear to be temperature activated. The average value of the permittivity is 37, compared to 10 for the a-axis measurement: −40 °C, blue squares; −10 °C, red diamonds; 20 °C, green triangles; 50 °C, purple circles; and 90 °C, light blue circles. The inset shows the temperature dependence of the dielectric permittivity, measured at individual frequencies. There is a continual rise in the permittivity as the temperature is increased: 1 154 500 Hz, blue squares; 316 110 Hz, red diamonds; 6488.6 Hz, green triangles; 205.11 Hz, purple circles; 15.377 Hz, light blue circles; and 0.748 54 Hz, orange squares.

hundred picoseconds (e.g., 100 ps for a HWHM equal to 6.5 μeV). These values indicate water diffusion dynamics that are much slower compared to not only bulk water (characterized by picosecond dynamics at ambient temperature), but also water confined in larger Vycor pores [43]. In contrast, the QENS broadening values obtained for water in much tighter confinement in zeolites NaA, NaX, and NaY [22,24] was also on the μeV scale, indicating the presence of dynamics on a time scale similar to that observed in our experiment.

C. Dielectric spectroscopy

As noted above, DS measurements were made on this sample parallel to the a and c axes, as was done with the INS and QENS experiments, providing data on lower-frequency (10^6–10^{-1} Hz, 10^{-6}–10 s) collective motions of the water dipoles. The dielectric losses for the a axis are presented in Fig. 13. For the c axis the dielectric losses are small and very noisy, so it is better to consider the dielectric relaxations (Fig. 14). By comparing the two data sets it is immediately evident that there exists a strong anisotropy in the crystal. The average value of the real component of the dielectric permittivity in the c axis direction is 37, compared to 10 in the a-axis direction. These values can be compared to the literature values for dry beryl reported by Keller (6.16–6.18 along the c axis and 5.67–6.59 along the a axis in the GHz range) [73] and by Singh and Prakash [74] (7.67–7.03 along c axis in the frequency range from 100 kHz to 20 MHz). The discrepancy between these literature values and our measurements can be explained by the presence of water trapped in the crystal structure. Furthermore the existence of a pronounced low-frequency tail in the dielectric landscape of the c axis points to processes happening on time scales far below the frequency window of the measurement. The inset of Fig. 14 demonstrates that at all frequencies measured there is a gradual increase in the strength of the process with temperature. This is consistent with a slow transport process.

More information on the dipolar state of the crystal is available on the a axis. The dielectric losses in this direction demonstrate a weak temperature-activated relaxation process, combined with a low-frequency tail. In this case it is possible to fit the process using the following composite dielectric function:

$$\varepsilon^*(\omega) = \varepsilon_\infty + \frac{\Delta\varepsilon}{1+(i\omega\tau)^\alpha} + B(i\omega)^{-n} + \frac{\sigma_{\rm dc}}{i\omega\varepsilon_0}, \qquad (9)$$

where ε_∞ is the high-frequency limit of the permittivity. The second term of Eq. (9) is usually referred to as a Cole-Cole function [56,75], $\Delta\varepsilon$ is the dielectric strength of the process, τ is the characteristic relaxation time, ω is the cyclic frequency, and α is a parameter between 0 and 1 that accounts for the broadening of the dielectric relaxation peak. The low-frequency tail on the a axis is fitted parametrically in the third term of Eq. (9) as a left-hand Jonscher process [55,76], where B is the amplitude of the tail and n accounts for its power-law behavior. Finally, the fourth term in Eq. (9) models a dc conductivity component in the data, accounted for by $\sigma_{\rm dc}$, where ε_0 is the permittivity of free space (8.85×10^{-12} F/m).

The results of this fitting are presented in Figs. 15–18. Figure 15 presents the relaxation times as a function of inverse temperature (an Arrhenius plot). The straight-line dependence conforms to the Arrhenius law $\tau = \tau_0 \exp(\Delta E/kT)$, giving an energy of activation for the dipole reorientation of 16.4 ±

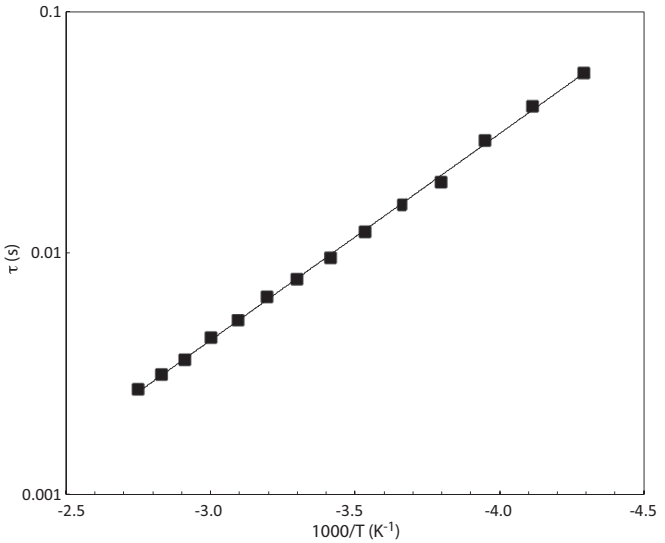

FIG. 15. Arrhenius plot of the temperature dependence of the relaxation times for the temperature-activated process measured in the a-axis orientation. The derived energy of activation suggests a process depending on the breaking of one H bond (in bulk water the energy of activation associated with the breaking of one H bond is 20 kJ/mol). This suggests that the process involves the gradual rotation of a single water molecule in the plane of the a axis (rotation axis approximately parallel to the c-axis channels).

0.14 kJ/mol. The energy typically required to break a hydrogen bond in bulk water is approximately 20 kJ/mol [77] and thus our result suggests that this process may involve H-bond activation. If so, then it points to the reorientation of a water molecule in the channel as the source of this process. If one considers the unit cell diagram (Fig. 1), the channel can be viewed as consisting of stepped rings of oxygen atoms with six atoms in each ring. A water molecule situated inside such a channel could form H bonds with these rings, while concurrently suffering a repulsion between the ring and the

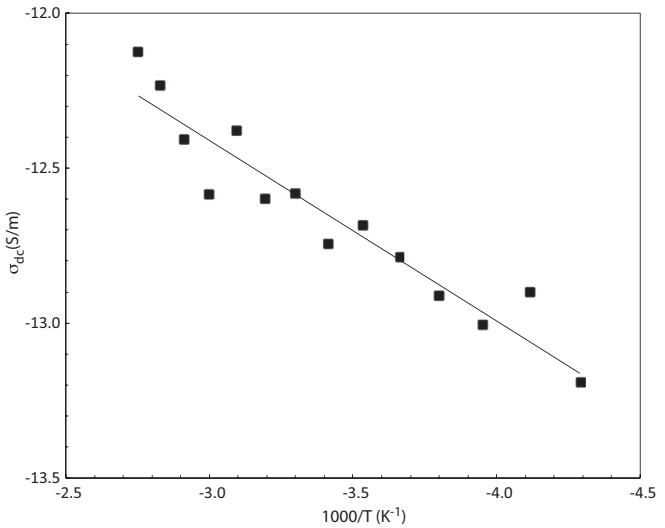

FIG. 16. Temperature dependence of dc conductivity in Arrhenius coordinates, measured in the a-axis direction. The source of dc conductivity is most likely residual lattice defects.

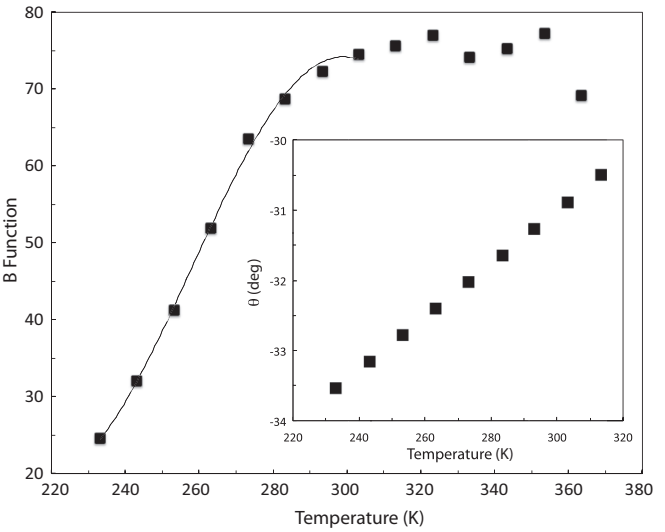

FIG. 17. Fröhlich B function for the a-axis process. The solid line is a fitting to the B function expressed as a $B_m(1 + z\cos\theta)$ dependence. The inset shows the variation of the angle θ as a function of temperature in the region of the fitting.

oxygen of the water molecule. The stepped nature of the ring structure would lead to consecutively tilted water molecules, whereby the H atoms of one water molecule aligns with the oxygen of the next. The a-axis process thus results from a reorientation of a water molecule in the plane of the ring, while the tilted structure leads to an overall strong dielectric strength on the c axis. This is consistent with known IR data for type-I water in alkali-metal-free beryls, which indicate that the water structure is dominated by parallel-aligned molecules along the channel [31,78]. This is schematically represented in Fig. 19. However, the INS spectra show no evidence of the presence of hydrogen bonding acting on the water in the beryl channels, suggesting that this represents some other interaction (e.g., ionic and/or van der Waals bonding), but the resolution of this apparent contradiction remains uncertain.

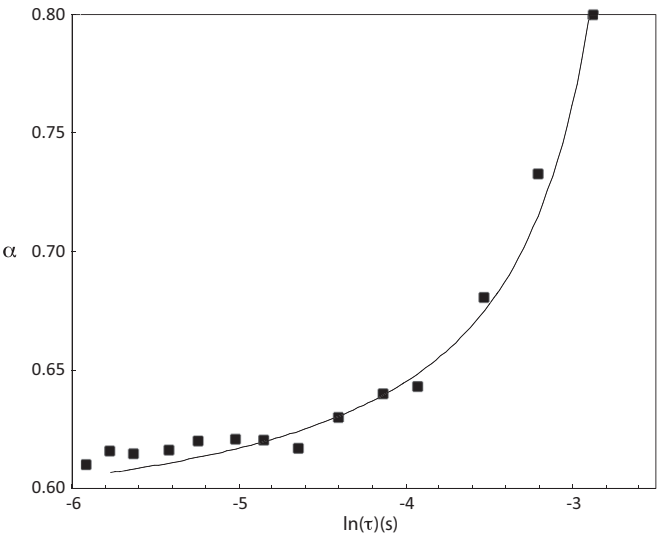

FIG. 18. The α (τ) dependences for the a-axis process. The solid line is the fitting function (12).

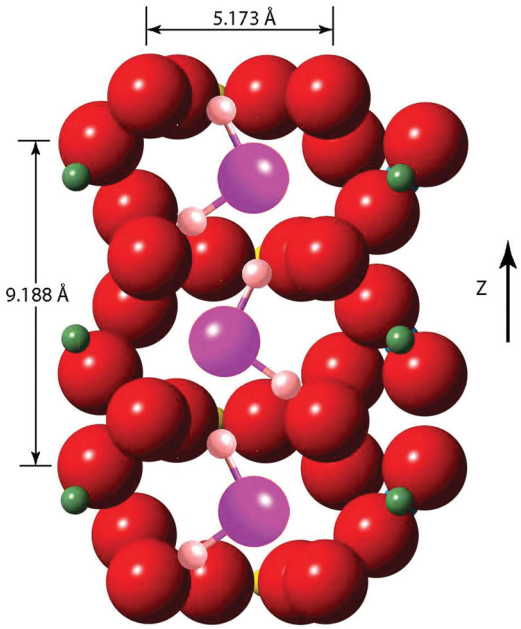

FIG. 19. (Color) Graphical representation of the alignment of water molecules inside the channels, giving rise to the anisotropic dielectric values in the c axis compared to those of the a axis: beryl oxygen, red; water oxygen, dark pink; water hydrogen, light pink; beryllium, green; and silicon, yellow.

Surprisingly, there is also a dc conductivity along the a axis (Fig. 16). While small, averaging less than 10^{-12} S/m, it shows a measurable temperature dependence with an activation energy of 11.15 $\pm$0.77 kJ mol^{-1}. While it is not possible to pinpoint the source of this conductivity precisely, it is most likely due to defect migration in the crystalline lattice.

One can gain further insight if one considers the Fröhlich B function [79,80]. The Fröhlich B function estimates the correlation between the relaxing dipole and the average dipole direction in the system under consideration. It is given by

$$B(T) = \Delta\varepsilon \frac{2\Delta\varepsilon + 3\varepsilon_\infty}{3(\Delta\varepsilon + \varepsilon_\infty)} T, \tag{10}$$

where the parameters are as defined above. The correlation can be expressed in terms of the average angle θ between the test dipole and the average dipole moment of the system and so Eq. (10) can be equated with

$$B(T) = \frac{n_0}{\varepsilon_0 3k} \langle \boldsymbol{m}\boldsymbol{m}^* \rangle = B_m(1 + z\,\langle \cos\theta \rangle), \tag{11}$$

where n_0 is the dipole density, ε_0 is the permittivity of free space, k is Boltzmann's constant, $\boldsymbol{m}^*$ is the averaged single dipole moment vector of the system, and $\boldsymbol{m}$ is the moment of a single dipole. The angular brackets denote thermal averaging, z is the number of nearest neighbors to the dipole in question, and $B_m \equiv \frac{n_0}{\varepsilon_0 3k} m^2$. The advantage of the $B(T)$ function is that it is calculable from the readily accessible experimental parameters. The $B(T)$ for the a-axis process is shown in Fig. 17. For temperatures up to 300 K $B(T)$ follows Eq. (11), with the angle given by $\theta = \pi A(T - T_0)$, where $A = 0.012 \pm 0.001$ K^{-1} and $T_0 = 1122 \pm 73$ K. Here T_0 is reasonably close to the temperature ($\sim$1045 °C, 1318 K) at which there was a significant weight loss during the thermogravimetry experiment. As the angle is evidence of increased correlation between neighboring dipoles, two conclusions can be drawn: (i) The relaxing dipole is confirmed as water rather than a lattice defect and (ii) the increased correlation is the result of an interaction between the water molecule and the lattice structure, which finally results in the dehydration transition observed in the thermogravimetry experiment.

Above 300 K $B(T)$ plateaus at an average value of 75. From the fitting one can obtain $z = 0.59 \pm 0.09$, implying a correlation with at most one nearest neighbor. The amplitude B_m is 46.7 ± 1.3. Using the literature value of the dipole moment for water m =1.85 D [81], one may obtain the density of dipoles engaged in the relaxation. Fitting yields $n_0 = 4.5 \times 10^{26}$ m^{-3}. Beryl has a unit cell volume of 675.1 Å^3 and a cell content of 2 for the $Be_3Al_2Si_6O_{18}$ formula unit. When considered on the scale of the unit cell, therefore, this translates to n_0 =0.304 per unit cell or about 0.15 dipoles per formula unit. By comparison, the estimate from the electron probe estimate was 0.625 water molecules per formula unit, total thermogravimetry water loss yielded 0.54 water molecules per formula unit, and the high-temperature part of the thermogravimetry weight change yielded 0.41 water molecules per formula unit. In all cases, therefore, the number of dipoles estimated from the DS results is significantly smaller than that measured analytically. Therefore, one can conclude that only about 30% of the available water molecules are involved in the relaxation process.

The parameter α in Eq. (9) reflects the broadening of the peak in the dielectric losses. It has been shown to be related to the interaction of the relaxing dipole with the matrix that surrounds it [56,80,82]. This interchange can be expressed by the relationship between α and the relaxation time

$$\alpha = A + \frac{\ln N_0}{\ln\tau - \ln\tau_0}. \tag{12}$$

This is illustrated in Fig. 18. Equation (12) is derived from a more fundamental expression relating α as a fractal dimension expressing the scaling relationship between the number of elemental relaxations N occurring during a particular time scale τ bounded by a minimum time scale of τ_0, $\alpha = \ln N/\ln\xi$, where $\xi = \tau/\tau_0$ [80]. While a full explanation of this expression is beyond the scope of this paper, the results of the fitting are $A = 0.57 \pm 0.01$, $\ln N_0 = -0.12 \pm 0.04$, and $\tau_0 = 0.09 \pm 0.01$ s. The parameter A is the asymptotic value of α at small τ, representing the boundary of possible self-scaling, the limit at which relaxation behavior can no longer be considered collective. At this minimum mesoscopic scale (the single channel), the rate of relaxations per second is given by $N_0/\tau_0 = 9.8$, pointing to a very weak relaxation process. This is confirmed by the correlation analysis provided from the Fröhlich B function above.

VI. CONCLUSION

The goal of this study was to analyze the directional dependence of the dynamics of water ultraconfined in the close-to-one-dimensional environment of the channels in the

beryl structure using single-crystal samples of beryl oriented in different ways with respect to the probe. As there are a number of processes involved, which occur with a wide range of relaxation times, we used three techniques, INS, QENS, and DS, to investigate a wide range of frequencies.

In the INS experiment the shift in the observed O-H stretch at the highest frequencies relative to those observed in any other type of water or ice suggested that there were no hydrogen bonds acting on the water molecule. These data also showed, somewhat surprisingly, that vibrations parallel to the *c*-axis channels were significantly more hindered than those perpendicular to it: the mean-square displacement was asymmetrical, larger in the direction perpendicular to the *c*-axis than along it; splitting of the intramolecular scissors mode in the Q-parallel orientation suggested that the water molecules were more strongly bound, and not free to vibrate, perpendicular to the O—H bond. Higher backgrounds suggested more intensity of low-energy modes perpendicular to the *c* axis and the overall inelastic results showed that water protons experienced a softer effective potential perpendicular, not parallel, to the *c* axis. This is in accord with optical spectrographic results [67]. However, the INS data disagree with their assumption that there are hydrogen bonds acting on the water molecules similar to those observed in water and ice. The INS data show no evidence for the presence of such bonding.

The QENS experiment also observed anisotropy in microscopic diffusion dynamics of water molecules ultraconfined in the channels. The dynamics observed by QENS at ambient temperatures and above appear to be primarily translational, but, again counterintuitively, the diffusion process is more hindered in the direction along the channels, in which direction it appears to have a single-file character, as opposed to the regular diffusion process observed perpendicular to the channel's axes, which may be related to a rotation or other reorientation of the molecule in the plane perpendicular to the *c* axis. Below approximately 150 K, there is evidence of the strong suppression (freezing out) of the diffusion along the channels, but no such suppression has been observed in the channel-perpendicular direction. It should be noted that this frozen out (in the direction parallel to the channels) state of the sample was probed in the INS experiment, which was performed at low temperature.

Slower, cooperative dynamics observed in the DS experiment in a temperature range more comparable with the QENS measurements than the low-temperature INS measurements were also strongly anisotropic. The dielectric permittivity (and therefore the electric flux) was lower perpendicular to the *c* axis than along it. Data along the *c* axis suggest a weak-temperature-activated relaxation process, along with some process at rates even slower than those investigated here. Processes along the *a*-axis direction were, however, faster, and quantifiable within the frequency range of the measurements. The temperature dependence of the relaxation times was Arrhenian, with an activation energy similar to that for breaking a hydrogen bond. This contrasts with the INS results that suggested no such bonds exist. From the observed stretching mode energy in the INS experiment (which is almost the same as for free water molecule) it follows that hydrogen bonding should be negligible or completely absent. This apparent discrepancy is discussed below. The *a*-axis DS results are consistent with reorientation in the plane of the ring, but with at most only short-distance correlation between the water dipoles.

Several observations thus lead us to the somewhat counterintuitive conclusion that, on the microscopic scale, confinement effects are more pronounced for diffusion along the channels. These include (i) the stronger Q dependence of the $x(Q)$ parameter in the QENS data in this direction, (ii) the single-file (as opposed to regular) diffusion process observed in this direction by QENS, (iii) the somewhat smaller average values of the QENS broadening in this direction, (iv) the low-temperature freezing out of the single-file diffusion process in this direction as suggested by the elastic intensity scans, (v) the harder effective potential in this direction as suggested by the INS data, and (vi) the differences in the dielectric permittivity parallel and perpendicular to the axis.

It should again be noted that, among the aforementioned effects, (iv) and (v) were detected in the low-temperature regime, where the possible freezing out of the dynamics in the *c*-parallel direction can be inferred from the low-temperature part of the elastic spectra in the QENS experiment, while (i)–(iii) and (vi) were measured at higher temperatures. The presence of the more pronounced confinement effects along the directions of the channels is in agreement with the DS data that show strong interactions for the water molecules in these directions. The QENS results suggest that the structure becomes much more rigid (the scattering becomes more elastic) in the *c*-parallel direction only as temperature decreases. The discrepancies between the INS (low-temperature) and DS (relatively-high-temperature) results could be attributed to this effect. That is, given the more crowded environment in the *c* direction, single-file QENS diffusion occurs at ambient temperature that freezes out at low temperatures, leading to more hindered vibrations.

As we have already mentioned, there appears to be a discrepancy between the INS data, which suggest that no hydrogen bonding is present, and the DS results, which suggest that bonding with an activation energy similar to that of a hydrogen bond is present in the *a*-axis direction. This may be a directional effect. A hydrogen bond is defined by both energetic and geometric constraints. Geometrically the bond is defined by the distance between the oxygen atom and the hydrogen atoms of the water molecule and the angle between the O-O vector and the covalent O—H bond, the first being defined as about 2.45 Å relative to simple point charge water and the latter within 30°–40° [83]. Thus the DS results may reflect relative bonding between the water molecule and the framework of the beryl that, being at a different angle, does not alter that OH stretching modes in the manner expected for a hydrogen bond. The lack of evidence for hydrogen bonding in the INS experiment also suggests that the perpendicular motion cannot be a consequence of proton hopping in an off-axis direction along the channels.

While the anisotropy of the macroscopic diffusion coefficients for fluids in confinement is well documented, this work provides experimental evidence of the anisotropy in the microscopic dynamics for water ultraconfined in quasi-one-dimensional channels. Results suggest, counterintuitively, that most observed dynamics are less hindered in directions perpendicular to the structural channels in the beryls. Further work is needed, however, to investigate the effects of variations in

channel dimensions and chemistry. In addition, deep inelastic neutron scattering measurements can be used to determine how ultraconfinement effects the zero point energy of the water molecule in the parallel and perpendicular directions and a comprehensive analysis of the low-energy part of the INS spectrum not investigated here would also provide data on possible tunneling behavior of water molecules in the perpendicular direction as suggested by optical spectroscopy [67].

ACKNOWLEDGMENTS

This research was sponsored by the Division of Chemical Sciences, Geosciences, and Biosciences, Office of Basic Energy Sciences, US Department of Energy. The neutron scattering experiment at Oak Ridge National Laboratory's Spallation Neutron Source was sponsored by the Scientific User Facilities Division, Office of Basic Energy Sciences, US Department of Energy. The authors would like to thank Professor Yuri Feldman for fruitful discussions on the implications of this paper, Dr. Ted Labotka and Allan Patchen of the University of Tennessee for providing the electron microprobe analysis, and Dr. Michelle Kidder of ORNL for the thermogravimetry analysis. Beryl crystals were cut by Bradley S. Wilson of Coast-to Coast Rarestones, International. We would also like to thank two anonymous reviewers for their efforts.

[1] A. I. Kolesnikov, J.-M. Zanotti, C.-K. Loong, P. Thiyagarajan, A. P. Moravsky, R. O. Loutfy, and C. J. Burnham, Phys. Rev. Lett. **93**, 035503 (2004).

[2] in *Micro- and Mesoporous Mineral Phases*. edited by G. Ferraris and S. Merlino, Reviews in Mineralogy and Geochemistry Vol. 57 (Mineralogical Society of America, Chantilly, VA, 2005).

[3] E. Mamontov, Yu. A. Kumzerov, and S. B. Vakhrushev, Phys. Rev. E **71**, 061502 (2005).

[4] E. Mamontov, Yu. A. Kumzerov, and S. B. Vakhrushev, Phys. Rev. E **72**, 051502 (2005).

[5] N. T. Skipper, P. A. Lock, J. O. Titiloye, J. Swenson, Z. A. Mirza, W. S. Howells, and F. Fernandez-Alonso, Chem. Geol. **230**, 182 (2006).

[6] J. Swenson, R. Bergman, and W. S. Howells, J. Chem. Phys. **113**, 2873 (2000).

[7] J. Swenson, R. Bergman, and S. Longeville, J. Chem. Phys. **115**, 11299 (2001).

[8] L. J. Michot, A. Delville, B. Humbert, M. Plazanet, and P. Levitz, J. Phys. Chem. C **111**, 9818 (2007).

[9] V. Marry, N. Malikova, A. Cadene, E. Dubois, S. Durand-Vidal, P. Turq, J. Breu, S. Longeville, and J. M. Zanotti, J. Phys.: Condens. Matter **20**, 104205 (2008).

[10] N. Malikova, A. Cadene, E. Dubois, V. Marry, S. Durand-Vidal, P. Turq, J. Breu, S. Longeville, and J. M. Zanotti, J. Phys. Chem. C **111**, 17603 (2007).

[11] N. Malikova, A. Cadene, V. Marry, E. Dubois, and P. Turq, J. Phys. Chem. B **110**, 3206 (2006).

[12] E. Mamontov, J. Chem. Phys. **121**, 9087 (2004).

[13] E. Mamontov, J. Chem. Phys. **123**, 024706 (2005).

[14] E. Mamontov, J. Chem. Phys. **123**, 171101 (2005).

[15] E. Mamontov, L. Vlcek, D. J. Wesolowski, P. T. Cummings, J. Rosenqvist, W. Wang, D. R. Cole, L. M. Anovitz, and G. Gasparovic, Phys. Rev. E **79**, 051504 (2009).

[16] E. Mamontov, L. Vlcek, D. J. Wesolowski, P. T. Cummings, W. Wang, L. M. Anovitz, J. Rosenqvist, C. M. Brown, and V. G. Sakai, J. Phys. Chem. C **111**, 4328 (2007).

[17] E. Mamontov, D. J. Wesolowski, L. Vlcek, P. T. Cummings, J. Rosenqvist, W. Wang, and D. R. Cole, J. Phys. Chem. C **112**, 12334 (2008).

[18] P. D. Shepherd, W. W. Kagunya, C. I. Campbell, A. P. Chapple, J. W. Dreyer, R. J. Humphreys, M. Kemali, M. Mercer, and D. K. Ross, Physica B **234–236**, 914 (1997).

[19] H. Paoli, A. Methivier, H. Jobic, C. Krause, H. Pfeifer, F. Stallmach, and J. Karger, Micropor. Mesopor. Mater. **55**, 147 (2002).

[20] W. A. Kamitakahara and N. Wada, Phys. Rev. E **77**, 041503 (2008).

[21] P. Demontis, J. Gulin-Gonzalez, M. Masia, and G. B. Suffritti, J. Phys.: Condens. Matter **22**, 284106 (2010).

[22] P. Demontis, H. Jobic, M. A. Gonzalez, and G. B. Suffritti, J. Phys. Chem. C **113**, 12373 (2009).

[23] J. Sinkankas, *Emerald and Other Beryls* (Geoscience, Tucson, 1994).

[24] D. L. Wood and K. Nassau, Am. Mineral. **53**, 777 (1968).

[25] P. Cerny, Neues Jb. Miner. Abh. **123**, 198 (1975).

[26] F. C. Hawthorne and P. Cerny, Can. Mineral. **15**, 414 (1977).

[27] P. Cerny and F. M. Simpson, Can. Mineral. **15**, 489 (1977).

[28] G. E. Brown, Jr. and B. A. Mills, Am. Mineral. **71**, 547 (1986).

[29] G. Artioli, R. Rinaldi, K. Stahl, and P. F. Zanazzi, Am. Mineral. **87**, 762 (1993).

[30] C. Aurisicchio, G. Fioravanti, O. Grubessi, and P. F. Zanazzi, Am. Mineral. **73**, 826 (1988).

[31] C. Aurisicchio, O. Grubessi, and P. Zecchini, Can. Mineral. **32**, 55 (1994).

[32] R. R. Viana, H. Jordt-Evangelista, G. Magela da Costa, and W. B. Stern, Phys. Chem. Miner. **29**, 668 (2002).

[33] A. A. Levchenko, A. I. Kolesnikov, N. L. Ross, J. Boerio-Goates, B. F. Woodfield, G. Li, and A. Navrotsky, J. Phys. Chem. A **111**, 12584 (2007).

[34] A. I. Kolesnikov, H. X. Yang, Y. G. Shi, J. Q. Li, R. I. Walton, and J. Li, Phys. Rev. B **76**, 092302 (2007).

[35] J.-M. Zanotti, M.-C. Bellissent-Funel, and A. I. Kolesnikov, Eur. Phys. J. Spec. Top. **141**, 227 (2007).

[36] D. Russo, J. Teixeira, L. Kneller, J. R. D. Copley, J. Ollivier, S. Perticaroli, E. Pellegrini, and M. A. Gonzalez, J. Am. Chem. Soc. **133**, 4882 (2011).

[37] A. J. Dianoux, F. Volino, and H. Hervet, Mol. Phys. **30**, 1181 (1975).

[38] D. J. Cebula, R. K. Thomas, and J. W. White, Clays Clay Miner. **29**, 241 (1981).

[39] F. Volino, M. Pineri, A. J. Dianoux, and A. de Geyer, J. Polym. Sci. B **20**, 481 (1982).

[40] J. J. Tuck, P. L. Hall, M. H. B. Hayes, D. K. Ross, and C. Poinsignon, J. Chem. Soc. Faraday Trans. **80**, 309 (1984).

[41] C. Poinsignon, H. Estrade-Szwarckopf, J. Conard, and A. J. Dianoux, Physica B **156–157**, 140 (1989).
[42] M.-C. Bellissent-Funel, K. F. Bradley, S. H. Chen, J. Lal, and J. Teixeira, Physica A **201**, 277 (1993).
[43] M.-C. Bellissent-Funel, S. H. Chen, and J.-M. Zanotti, Phys. Rev. E **51**, 4558 (1995).
[44] M.-C. Bellissent-Funel, J. Teixeira, K. F. Bradley, and S. H. Chen, J. Phys. I. France **2**, 995 (1992).
[45] M.-C. Bellissent-Funel, J. Teixeira, K. F. Bradley, S. H. Chen, and H. L. Crespi, Physica B **180–181**, 740 (1992).
[46] M.-C. Bellissent-Funel, J.-M. Zanotti, and S. H. Chen, Faraday Discuss. **103**, 281 (1996).
[47] U. Wanderlingh, R. Giordano, and J. Teixeira, J. Mol. Struct. **296**, 271 (1993).
[48] R. E. Lechner, N. A. Dencher, J. Fitter, and T. Dippel, Solid State Ion. **70–71**, 296 (1994).
[49] R. E. Lechner, N. A. Dencher, J. Fitter, G. Buldt, and A. V. Belushkin, Biophys. Chem. **49**, 91 (1994).
[50] M. Settles and W. Doster, Faraday Discuss. **103**, 269 (1996).
[51] T. Takamuku, M. Yamagami, H. Wakita, Y. Masuda, and T. Yamaguchi, J. Phys. Chem. B **101**, 5730 (1997).
[52] S. Takahara, M. Nakano, S. Kittaka, Y. Kuroda, T. Mori, H. Hamano, and T. Yamaguchi, J. Phys. Chem. B **103**, 5814 (1999).
[53] S. Dellerue and M.-C. Bellissent-Funel, Chem. Phys. **258**, 315 (2000).
[54] M. Gay-Duchosal, D. H. Powell, R. E. Lechner, and B. Ruffle, Physica B **276–278**, 234 (2000).
[55] F. Kremer and A. Schönhals, *Broadband Dielectric Spectroscopy*, 1st ed. (Springer, Berlin, 2002).
[56] Y. Feldman, A. Puzenko, and Y. Ryabov, in *Fractals, Diffusion and Relaxation in Disordered Complex Systems*, edited by W. T. Coffey and Yu. P. Kalmykov, Advances in Chemical Physics Vol. 133 (Wiley, New York, 2006), Pt. A, pp. 1–125.
[57] R. Pankrath and K. Langer, Am. Mineral. **87**, 238 (2002).
[58] G. E. Granroth, A. I. Kolesnikov, T. E. Sherline, J. P. Clancy, K. A. Ross, J. P. C. Ruff, B. D. Gaulin, and S. E. Nagler, J. Phys. Conf. Ser. **251**, 012058 (2010).
[59] http://www.mantidproject.org.
[60] E. Mamontov and K. W. Herwig, Rev. Sci. Instrum. **82**, 085109 (2011).
[61] K. Hahn, H. Jobic, and J. Karger, Phys. Rev. E **59**, 6662 (1999).
[62] Novocontrol, User's Manual: Alpha High Resolution Dielectric Analyser (Novocontrol GmbH, Hundsangen, 2000).
[63] A. I. Kolesnikov (unpublished).
[64] J. Li and A. I. Kolesnikov, J. Mol. Liquids **100**, 1 (2002).
[65] A. Janca, K. Tereszchuk, P. F. Bernath, N. F. Zobov, S. V. Shirin, O. L. Polyansky, and J. Tennyson, J. Mol. Spectrosc. **219**, 132 (2003).
[66] R. Lemus, J. Mol. Spectrosc. **225**, 73 (2004).
[67] B. P. Gorshunov, E. S. Zhukova, V. I. Torgashev, V. V. Lebedev, G. S. Shakurov, R. K. Kremer, E. V. Pestrjakov, V. G. Thomas, D. A. Fursenko, and M. Dressel, J. Phys. Chem. Lett. **4**, 2015 (2013).
[68] C. Andreani, D. Colognesi, J. Mayers, G. F. Reiter, and R. Senesi, Adv. Phys. **54**, 377 (2005).
[69] M. Bee, *Quasielastic Neutron Scattering* (Hilger, Bristol, 1988).
[70] S.-H. Chen, C. Liao, F. Sciortino, P. Gallo, and P. Tartaglia, Phys. Rev. E **59**, 6708 (1999).
[71] E. Mamontov, H. M. Luo, and S. Dai, J. Phys. Chem. B **113**, 159 (2009).
[72] P. Demontis, G. Stara, and G. Suffritti, J. Phys. Chem. B **107**, 4426 (2003).
[73] G. V. Keller, in *Electromagnetic Methods in Applied Geophysics*, Vol. 1: Theory, edited by M. Nabighian (SEG Books, Tulsa, 1988), Chap. 2, pp. 13–48.
[74] J. Singh and P. K. Singh, Pure Appl. Geophys. **135**, 601 (1991).
[75] K. S. Cole and R. H. Cole, J. Chem. Phys. **9**, 341 (1941).
[76] A. K. Jonscher, *Universal Relaxation Law* (Chelsea Dielectrics, London, 1995).
[77] R. C. Dougherty, J. Chem. Phys. **109**, 7372 (1998).
[78] R. D. Aines and G. R. Rossman, Am. Mineral. **69**, 319 (1984).
[79] H. Frohlich, *Theory of Dielectrics: Dielectric Constant and Dielectric Loss*, 2nd ed. (Oxford University Press, New York, 1987).
[80] A. Puzenko, P. B. Ishai, and Y. Feldman, Phys. Rev. Lett. **105**, 037601 (2010).
[81] S. L. Shostak, W. L. Ebenstein, and J. S. Muenter, J. Chem. Phys. **94**, 5875 (1991).
[82] Y. E. Ryabov and Y. Feldman, Physica A **314**, 370 (2002).
[83] A. Luzar, J. Chem. Phys. **113**, 10663 (2000).